Journal of Nuclear Materials 508 (2018) 530–539

Contents lists available at ScienceDirect

Journal of Nuclear Materials

journal homepage: www.elsevier.com/locate/jnucmat

Effects of the short-range repulsive potential on cascade damage in iron

J. Byggmästar*, F. Granberg, K. Nordlund

Department of Physics, P.O. Box 43, FI, 00014, University of Helsinki, Finland

ARTICLE INFO

Article history:
Received 10 April 2018
Received in revised form
30 May 2018
Accepted 4 June 2018

Keywords:
Interatomic potential
Threshold displacement energy
Molecular dynamics
Iron
Collision cascade

ABSTRACT

Recent work has shown that the repulsive part of the interatomic potential at intermediate atomic separations strongly affects the extent and morphology of the damage produced by collision cascades in molecular dynamics simulations. Here, we modify an existing embedded atom method interatomic potential for iron to more accurately reproduce the threshold displacement energy surface as well as the many-body repulsion at intermediate and short interatomic distances. Using the modified potential, we explore the effects of an improved repulsive potential on the primary damage production and the cumulative damage accumulation in iron. We find that the extent of the damage produced by single cascades, in terms of surviving Frenkel pairs, directly correlates with the change in threshold displacement energies. On the other hand, the damage evolution at higher doses is more dependent on the formation and stability of different defect clusters, defined by the near-equilibrium part of the interatomic potential.

1. Introduction

Atomistic simulations have during the last decades been a widely used tool for studying radiation damage production on the atomic level. In metals, the development of accurate embedded atom method (EAM) [1] interatomic potentials has opened the possibility to extract more and more quantitative information from atomistic simulations. EAM potentials rely on the principles of density functional theory, and have been successful in describing near-equilibrium properties of metals and metal alloys [2,3]. However, when modelling radiation damage, the atomic system is pushed far from its equilibrium crystalline state, which consequently sets high demands on the interatomic potential.

Interatomic potentials for radiation damage studies require not only a good description of the equilibrium properties, but also a realistic description of short-range forces experienced as atoms with high velocities move through the lattice. Ziegler et al. have showed that the repulsive potential for any atom pair can be fairly accurately described by a universal potential in the form of a screened Coulomb potential [4]. When developing interatomic potentials applicable for radiation damage simulations, it has long been a standard approach to let this universal ZBL potential describe the repulsive interactions at short interatomic distances (below around 1 Å) [5–7]. However, the ZBL potential must be smoothly connected to the given near-equilibrium potential, be it an EAM potential, a Tersoff potential [8] or any other many-body potential. The transition between the ZBL and the equilibrium potential is typically achieved by a simple function defining the intermediate repulsive range [6]. This intermediate range can be tuned to reproduce the correct threshold displacement energies (TDEs). The combined potential then makes it possible to accurately model both highly repulsive forces and near-equilibrium properties, both which are important when simulating the evolution of a radiation damage event in a material. However, recent work [7,9] has shown that using the TDEs as the only criterion when fitting the intermediate transition part can still result in widely different potentials with large differences in radiation damage results. More emphasis should therefore be put on fitting the transition range.

Recently, radiation damage modelling has also focused on the damage produced by cascades overlapping with pre-existing damage, and the evolution of the defect structures at higher damage doses [10–13]. The rate of damage accumulation and clustering of point defects in overlapping cascades is dependent on the repulsive part of the potential. Furthermore, the types of defect clusters produced at higher doses, and their stability and evolution

* Corresponding author.
E-mail address: jesper.byggmastar@helsinki.fi (J. Byggmästar).

https://doi.org/10.1016/j.jnucmat.2018.06.005

after subsequent collision cascades, is dependent on the energetics of the defect clusters given by the interatomic potential. However, little attention has been paid to the resulting differences in the higher-dose cascade damage due to differences in the interatomic potential.

In this work, we adjust an existing EAM potential for iron [14,15] to more accurately reproduce experimental and *ab initio* data sensitive to the intermediate repulsive range of the potential. We use the modified potential in collision cascade simulations to explore the effects of different short-range potentials in both single and overlapping cascade simulations. We compare the results to another well-established potential [16]. The observed differences are discussed in relation to the specific features of the potentials.

2. Methods

2.1. Fitting the repulsive potential

The original parametrisation of the iron potential by Marinica et al. [14,15] (denoted M07) was found to predict TDEs significantly higher than experimental and *ab initio* data.[1] However, it provides a description of the equilibrium and point defect properties on par or better than other established iron potentials [14]. Furthermore, it is the only potential to our knowledge that correctly reproduces the relative stability of the C15 Laves phase clusters in body-centered cubic (bcc) iron compared to parallel interstitial configurations [15]. Therefore, we modify the pair potential part with the aim to reproduce TDEs and repulsive many-body potential curves more comparable to experimental and *ab initio* data. This is done while maintaining the good formation and migrational energies for interstitials and interstitial clusters given by the original potential. Using a previously adopted approach [6], we connect the ZBL potential (V_{ZBL}) and the near-equilibrium part ($V_{\mathrm{orig.}}$) with a polynomial function, and write the new pair potential as

$$V(r) = \begin{cases} V_{\mathrm{ZBL}}, & r \le r_1 \\ \sum_{n=0}^{7} a_n r^n, & r_1 < r < r_2 \\ V_{\mathrm{orig.}}, & r \ge r_2. \end{cases} \tag{1}$$

The ZBL potential [4] for an atom pair ij is given by

$$V_{\mathrm{ZBL}}(r_{ij}) = \frac{1}{4\pi\varepsilon_0}\frac{Z_i Z_j e^2}{r_{ij}}\phi(r_{ij}/a), \tag{2}$$

where the screening function is $\phi(x) = 0.18175e^{-3.19980x} + 0.50986e^{-0.94229x} + 0.28022e^{-0.4029x} + 0.02817e^{-0.20162x}$ and the screening length is $a = 0.4685/(Z_i^{0.23} + Z_j^{0.23})$. We note that the original potential and all other commonly used Ackland-Mendelev-like iron potentials [16–18] use the screening length by Lindhard et al. [19] instead of the standard ZBL screening length given above. The discrepancy is in the exponents of Z, but the resulting difference in potential energy is fairly minor in the case of Fe–Fe interactions. Nevertheless, in addition to replacing the intermediate transition function with a polynomial, we have also used the full ZBL potential at short-range interactions by replacing the Lindhard screening length with the standard ZBL screening length [4]. The transition polynomial function is smoothly connected to the ZBL and the equilibrium cubic spline function, making sure that the potential energy and its derivative are continuous across the transition points.

The original pairwise electron density function [14,15] grows continuously at short interatomic distances. In order for the ZBL potential to fully control the atomistic dynamics at low distances, we let the density function approach a constant value in the intermediate range defined by the polynomial pair potential. A constant electron density at short interatomic separations will only introduce a shift in the total potential energy given by the ZBL potential, and will therefore not change the dynamics governed by the interatomic forces [6]. The original density is smoothly forced to a constant value using a third-order polynomial function. The new density function is written

$$\psi(r) = \begin{cases} \psi_{\max}, & r \le R_1 \\ \sum_{n=0}^{3} A_n r^n, & R_1 < r < R_2 \\ \psi_{\mathrm{orig.}}, & r \ge R_2. \end{cases} \tag{3}$$

The repulsive potential fit was guided by calculating the threshold displacement energies and comparing them to experimental and *ab initio* data. TDEs in iron are sensitive to the repulsive potential at distances from around 2 Å down to about 1.4 Å. The ZBL potential has been shown to be accurate at around 1 Å and below [7]. Using only the TDEs to guide the fit therefore leaves an untested window in the 1–1.4 Å range. In order to subject the modified potential to the full range of interatomic distances from equilibrium distances down to the ZBL range, we performed quasi-static drag (QSD) simulations where an atom is stepwise moved along a chosen crystal direction in an otherwise fixed lattice. This method is similar to the sudden approximation method [20]. The QSD simulations are also sensitive to many-body interactions as the atom is moved through the lattice, and therefore serve as good tests for a potential. We compared the results to *ab initio* data by Olsson et al. [21], and could in this way adjust and choose a potential parametrisation that gave both satisfactory TDEs and a good agreement with the QSD energy curves from DFT. The pair potential was manually adjusted and the TDEs for all crystal directions were recalculated for every interatomic potential candidate. When a satisfactory agreement with the target data for the TDEs was achieved, we used the QSD energy curves to verify that the modified potential provides a reasonable description across the entire refitted range, in addition to the TDE-sensitive range.

From here on, we denote the modified M07 potential by M07-B. The results will be compared with the well-established potential by Ackland et al. [16], denoted as AM04.

2.2. Simulation methods

All molecular dynamics simulations were carried out using the classical MD code PARCAS [5,22]. Static energy minimisations and the quasi-static drag simulations were carried out using ASE [23] and LAMMPS [24]. The threshold displacement energies were calculated following the methods described in detail in Ref. [25]. Shortly, 5000 uniformly distributed random crystal directions were sampled using the polar angle θ and the azimuthal angle φ. For each direction, an atom was given increasingly higher kinetic energies until a stable Frenkel pair survived after a simulation time of 6 ps? The temperature of the system was 36 K, corresponding to the temperature used in the experiments in Ref. [26].

The single cascades were simulated with primary knock-on atom (PKA) energies in the range 1–100 keV at 0 K. The systems were cooled down and pressure waves from the cascade were damped by allowing heat to dissipate in the border regions using a Berendsen thermostat [27]. The time step was kept sufficiently short using the adaptive time step criterion from Ref. [28]. The simulation cell size was chosen to be large enough for the cascade not to interact with the thermally controlled border regions. Electronic stopping was applied to atoms with kinetic energies above

[1] The threshold displacement energies given in Ref. [14] for the M07 potential have been calculated with the wrong potential and are incorrect.

1 eV in the form of a friction term. The simulation time of the single cascades was 40 ps. For each energy, 50 individual simulations were carried out.

Higher damage doses were achieved by running 2500 overlapping cascades in the same simulation cell. The simulation cell size was $60 \times 63 \times 66$ unit cells in x-, y- and z-directions, respectively, resulting in ~ 500000 atoms. Each recoil event consisted of a single 5 keV cascade, resulting in a final dose of 0.15 dpa for the M07-B and AM04 potentials and a dose of 0.095 dpa in the M07 potential, according to the NRT-dpa equation [29].

$$N_\mathrm{d} = \frac{0.8T_\mathrm{d}}{2E_\mathrm{d}}, \quad T_\mathrm{d} > \frac{2E_\mathrm{d}}{0.8}. \tag{4}$$

Here, N_d is the number of defects produced by the damage energy T_d (i.e. the PKA energy minus the energy loss due to electronic stopping), and E_d is the threshold displacement energy. The dose values were calculated using the average threshold displacement energy for each potential. Three separate runs were conducted with each potential to assess the stochastic differences. All numerical results for the cascade overlap simulations given in Section 3 are the averages over the three different runs, unless otherwise specified. The simulations were carried out at room temperature (300 K) in order to capture some thermally activated effects, such as dislocation movement. Each cascade was simulated for 30 ps with a Berendsen thermostat applied to a few layers of atoms at the borders, to keep the temperature constant. The simulation time results in a dose rate many orders of magnitude higher than experimentally possible, but a similar simulation scheme has previously shown good agreement for the RBS/C (Rutherford backscattering spectrometry in channeling conditions) spectra of simulated and experimentally irradiated samples [30]. The simulation cell was shifted randomly after each cascade in all directions in order to obtain a homogeneous irradiation. The recoil was always initiated in the centre of the cell, to avoid interaction with the thermally controlled area, similarly to previous studies on other materials [12,13].

To study the nature of the produced defects, both in single and overlapping cascades, the Wigner-Seitz cell method was used to identify interstitials and vacancies [5]. The interstitials and vacancies were grouped into clusters by choosing the cutoff distances (i.e. the maximum distance between two defects for them to belong to the same cluster) as $(r_{2\mathrm{NN}} + r_{3\mathrm{NN}})/2$ for vacancies and $(r_{3\mathrm{NN}} + r_{4\mathrm{NN}})/2$ for interstitials, where $r_{i\mathrm{NN}}$ is the ith nearest neighbour distance. Dislocations were identified using the dislocation extraction algorithm (DXA) [31] implemented in OVITO [32].

3. Results and discussion

3.1. Repulsive potential fit

The pair potential smoothly transitions into the ZBL potential below an interatomic distance of 1 Å. The transition to the equilibrium cubic spline part was chosen to be at 2.05 Å, which is below the shortest distances for all common single interstitials and interstitial clusters. The modified potential therefore retains the good description of not only the equilibrium properties, but also the interstitial energetics predicted by the original M07 potential [14]. We verified this by calculating the formation energies of all common single interstitials as well as the migration energies of the main interstitial jumps with both the modified and the original potential, and obtained identical results. The modified pair potential is shown in Fig. 1 together with the original and the AM04 pair potential parts.

The melting temperature is overestimated in the M07 potential (2250 K [14] compared to the experimental value of 1811 K [33]). We also checked for possible changes in the predicted melting point due the modification, by determining the temperature at which a solid–liquid interface remains in equilibrium [34]. The obtained melting point of about 2250 K is identical to the value reported for the original potential in Ref. [14].

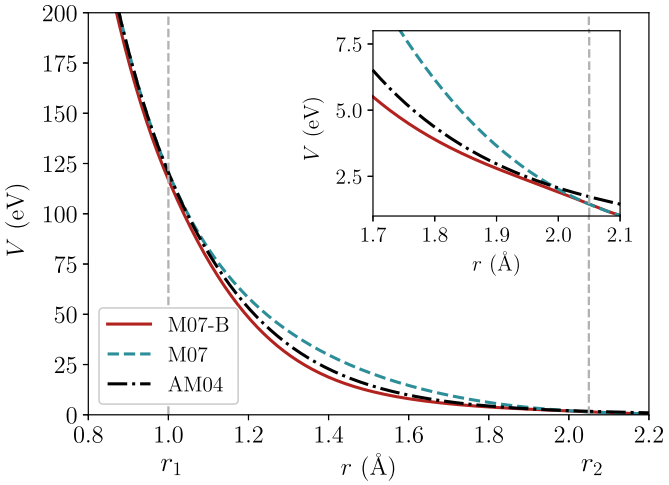

Fig. 1. The pair potential parts of the different potentials, illustrating the modification of the M07 potential below $r_2 = 2.05$ Å.

The modified pairwise density function smoothly approaches a constant value in the intermediate range as seen in Fig. 2. Again, the modification takes place on interatomic distances far below those relevant for interstitial clustering and migration, and has no effect on the point defect energetics or equilibrium properties. The new density function is shown and compared with the other potentials in Fig. 2. The fitted parameters of the polynomial transition functions in the modified pair potential and density function are given in Appendix A.

3.2. Tests of the modified potential

Table 1 shows the threshold displacement energies calculated with both the M07-B and the M07 potential, compared with the AM04 potential and experimental and *ab initio* data. When

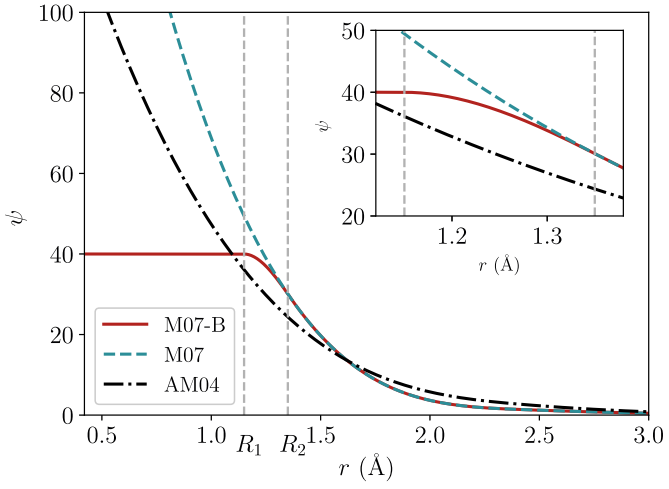

Fig. 2. The pairwise electron density functions of the different potentials, illustrating the modification made to the M07 potential to obtain the M07-B potential, by smoothly forcing the density to approach a constant value.

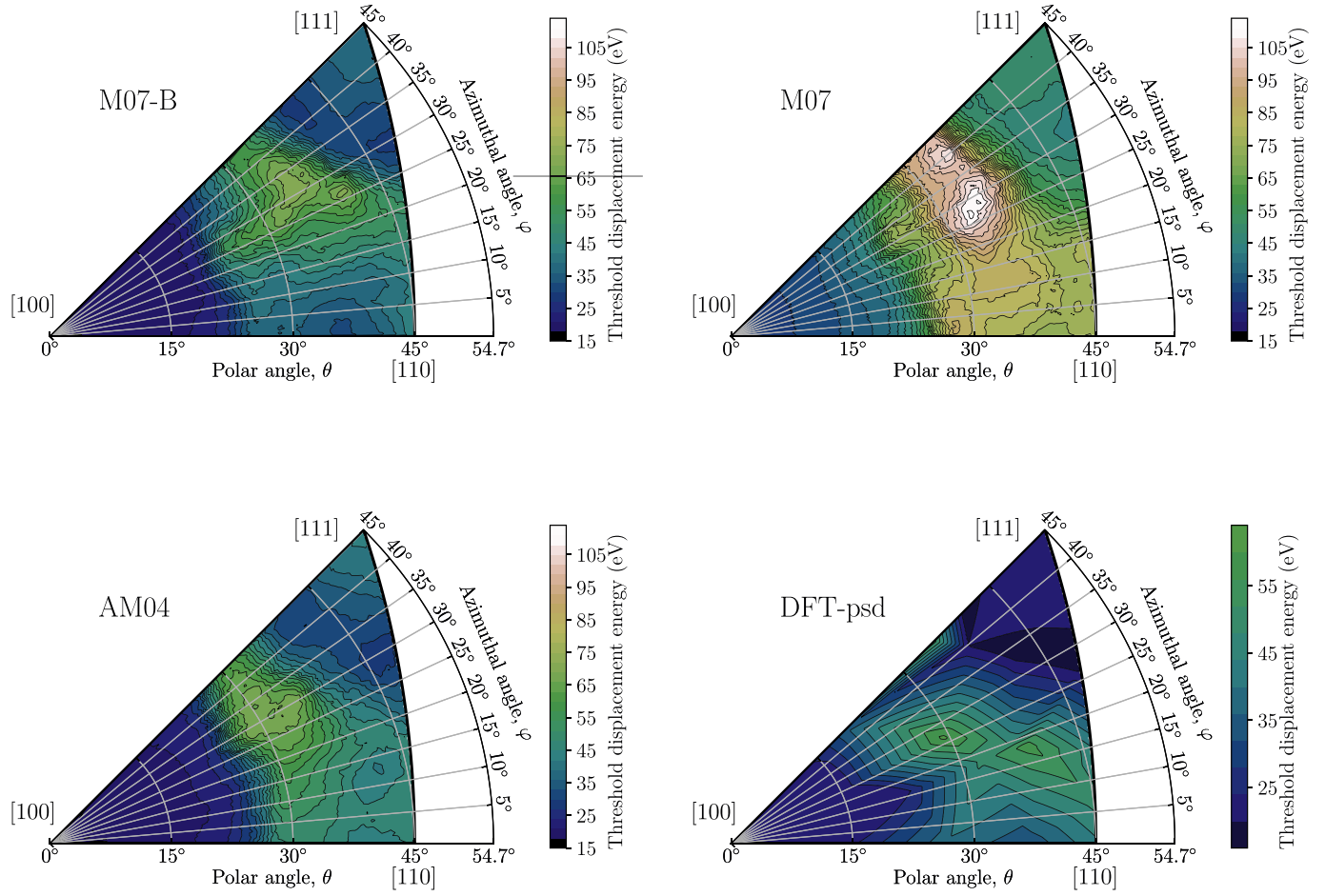

Fig. 3. Full angular maps of the threshold displacement energies for the modified potential (M07-B), the original potential (M07), the AM04 potential, and DFT data from Ref. [21]. The data points in the potential maps are the average values calculated within a 2° radius.

Table 1
Threshold displacement energies (in eV) predicted by the different potentials. δ is the angular radius around the different crystal directions within which the TDEs are obtained. The first line for each potential is the minimum TDE, and the second line is the average in the region defined by δ. The last column contains the average TDE values over all crystal directions. The uncertainties are the standard errors of the mean. The experimental and DFT values were used as targets when refitting the M07 pair potential part.

Potential	Crystal direction						Average
	⟨100⟩		⟨110⟩		⟨111⟩		
	$\delta = 2°$	$\delta = 5°$	$\delta = 2°$	$\delta = 5°$	$\delta = 2°$	$\delta = 5°$	
M07	27	27	51	51	43	43	
	29.0±0.5	29.3±0.2	75.3±1.8	77.2±1.2	50.6±1.8	50.7±0.4	65.5±0.3
M07-B	17	17	39	23	33	29	
	18.1±0.3	18.1±0.1	43.5±0.5	40.2±0.6	39.5±1.4	37.6±0.7	39.2±0.2
AM04	17	17	33	31	29	29	
	19.0±0.5	18.5±0.2	46.0±2.4	46.5±1.0	42.6±2.2	42.0±0.8	39.6±0.2
DFT-psd [21]		21		43		20	32
DFT-sd [21]		17		32		15	29
Exp. [26]		17		>30		20	
Exp. [35]		20		30			

calculating TDEs (experimentally or computationally), one must be careful with how the reported values for a given crystal direction are obtained, as the TDE surface is typically strongly anisotropic with possibly steep gradients and nearby local minima. The ambiguities in calculating and reporting TDE values are discussed in detail in Ref. [25]. For this reason, in addition to the values given in Table A.3, we show the full angular maps of the TDEs (averaged within a 2° radius around each point) calculated using the different potentials. The TDE maps are compared to the *ab initio* data from Ref. [21], obtained using both the standard electronic configuration (DFT-sd) and a harder semi-core potential (DFT-psd). Additionally, in Table 1 we give both the minimum and the average TDE values obtained within a 2° and 5° radius around the low-index crystal directions. The average values are more illustrative in case of strong gradients (like for the ⟨110⟩ directions), as the minimum values are dependent on the chosen angular tolerance around the exact direction. In particular, the average values compared to the minimum values provide an indication of the anisotropy around the given

crystal direction.

The angular TDE maps in Fig. 3 show the consistently overestimated TDEs for all crystal directions in the original M07 potential. The new M07-B potential is comparable to the AM04 potential, and both are overall in satisfactory agreement with the *ab initio* data. We note that the number of data points in the DFT-calculated TDE map is noticeably lower than the maps obtained in MD, however, some qualitative features can still be compared. A shortcoming of the EAM potentials is the inability to reproduce the low TDEs around the ⟨111⟩ directions, as discussed in Ref. [21]. A noteworthy difference between the M07-B and the AM04 potential can be seen in the [100]–[110] path, where the M07-B potential reproduces the soft minimum close to the [110] direction seen in the DFT data. The potentials are compared more quantitatively with the DFT data in Fig. 4, where the TDEs of the [100]–[110]–[111]–[100] path (along the edges of the angular maps) are plotted. The good agreement between the M07-B and DFT for the [100]–[110] path is clearly visible, while directions close to [111] are overestimated in both the M07-B and the AM04 potential. Again, Fig. 4 illustrates how the original M07 potential consistently overestimates all TDEs due to the stiffer pair potential in the TDE-relevant range.

As previously mentioned, quasi-static drag simulations provide good tests for how well the repulsive pair potential works together with the many-body potential for a wide range of interatomic distances and atomic environments. Fig. 5 shows the energy difference as the atom is moved along three crystal directions, calculated with the different potentials and compared to *ab initio* data from Ref. [21]. For translation along a ⟨111⟩ direction (towards the nearest neighbour atom), the opposing energy is mainly due to the pair interactions between the atom pair, and the resulting energy curve is essentially a comparison of the pair potential parts of the EAM potential with the DFT curve. The M07-B potential is in closest agreement with DFT. A similar curve is obtained for translation along a ⟨100⟩ direction, and is not shown here. For both the ⟨110⟩ and ⟨135⟩ directions, significant attractive many-body interactions are experienced as the atom moves past nearby surrounding atoms. The local maximum for the ⟨110⟩ direction corresponds to an octahedral interstitial site. The following local minimum is the point at which the target atom along the ⟨110⟩ path is at the same distance as the two other nearest neighbour atoms (the central atoms in the conventional bcc unit cell). Movement along a ⟨135⟩ direction produces similar local maxima and minima. The M07-B potential fairly accurately reproduces the energy response obtained by DFT in these directions, noticeably better than the AM04 potential. This can be considered a good validation of the accuracy of the M07-B potential across the entire refitted range. The effect of the softening of the M07 pair potential is also clear. The repulsive energies of the original potential M07 are too high, and softening of the pair potential brings the energy curves down to the levels predicted by DFT.

Earlier studies have suggested that the stiffness of the repulsive potential can be linked to certain features of the collision cascade and the resulting damage [36,37]. In iron, the stiffness has been characterised by the gradient (S) and interatomic distance (R) at which the pair potential energy is 30 eV [36]. A high $|S/R|$ ratio (i.e. a stiff potential) has been found to correlate with less dense cascade volumes and shorter relaxation times, and hence a low recombination efficiency for Frenkel pairs. A low $|S/R|$ ratio (i.e. a soft potential) was seen to generally lead to denser cascades with more damage at peak time, but also longer recombination times. The final amount of surviving Frenkel pairs was found to be controlled by the recombination efficiency in relation to the peak-time damage, and was seen to generally lead to similar surviving defect numbers for both stiff and soft potentials [37]. The stiffness parameters for the three potentials are given in Table 2. The M07-B potential is slightly stiffer, but comparable to the AM04 potential, while the original M07 potential is clearly softer. However, as seen in Fig. 1, the M07 potential is significantly stiffer than the other potentials in the 1.5–2.0 Å range, leading to high TDEs, but

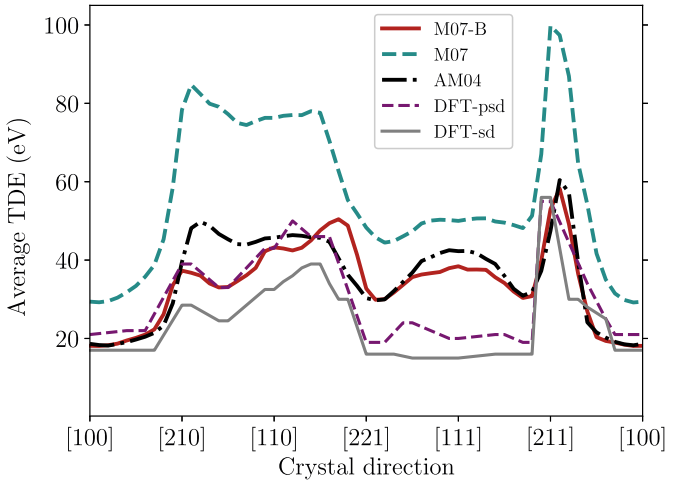

Fig. 4. Threshold displacement energies along the paths between the low-index crystal directions (along the edges of the maps in Fig. 3). The DFT data are from Ref. [21].

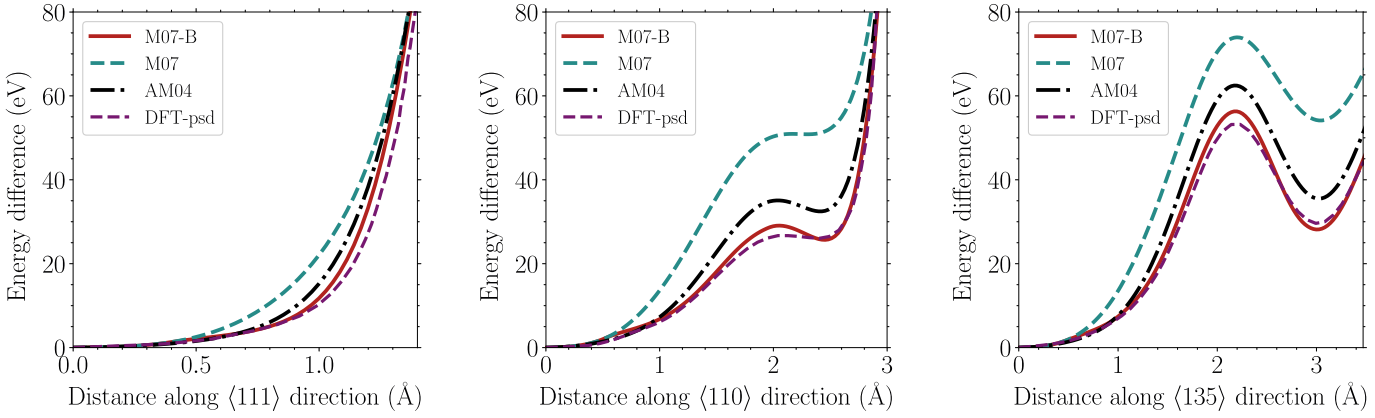

Fig. 5. Repulsive energy for an atom moving along different crystal directions in a rigid lattice. The DFT data are from Ref. [21].

Table 2
Values defining the stiffness of the different potentials.

	M07	M07-B	AM04
R (Å)	1.40	1.30	1.34
$\|S\|$ (eV/Å)	101.0	143.6	127.5
$\|S/R\|$ (eV/Å^2)	72.3	110.5	95.5

becomes softer below $\sim$ 1.5 Å, leading to 'softer' stiffness parameters according to the above-mentioned definition. The stiffness of the different potentials will be discussed in relation to the collision cascade damage studied in the following section.

3.3. Single cascade simulations

Fig. 6 shows the numbers of surviving Frenkel pairs after single cascades with energies from 1 keV to 100 keV. The M07-B potential produces significantly higher numbers of Frenkel pairs than the original M07 potential, with the AM04 results at intermediate numbers. The number of surviving Frenkel pairs is in the standard NRT damage model [29] inversely proportional to the threshold displacement energy. In order to explicitly see the effect of lowering the TDEs when fitting the M07-B potential, Fig. 6 also shows the number of Frenkel pairs as a function of the PKA energy divided by the average TDEs for each potential (as given in Table 1). At PKA energies below 20 keV, the TDE-normalised Frenkel pair numbers almost overlap for the M07-B and M07 potential, indicating that the increased cascade damage is entirely due to the change in the TDEs, as is assumed in the NRT-dpa model [29] as well as in the recent improved arc-dpa model [38]. Subcascade formation becomes increasingly stronger at PKA energies above 20 keV [37], which can explain the differences at higher energies. However, we note that the AM04 consistently predicts clearly lower numbers of Frenkel pairs than the M07-B potential across the studied PKA energy range, despite the average TDEs being almost identical in both potentials. The extent of the primary damage in terms of numbers of surviving vacancies and interstitials can therefore not be predicted solely based on the TDEs, but also depends on other factors.

As previously discussed, the stiffness of the repulsive part of the potential has been attributed to certain features in the primary damage in iron. The stiffness parameters in Table 2 shows that the M07-B is slightly stiffer than the AM04 potential, which in general results in lower damage at peak-time and shorter relaxation time for recombination. This is in line with our observations, i.e. the maximum damage in terms of Frenkel pairs during the evolution of a typical cascade is noticeably higher, and the relaxation time longer in the AM04 potential than in the M07-B potential. This is illustrated in Fig. 7, where the average defect count as a function of time is plotted for 10 keV cascades. Earlier we noted that the difference in surviving defect counts for PKA energies below the subcascade splitting threshold between the M07-B and the M07 potential can entirely be attributed to the difference in threshold displacement energy. In Fig. 7, we therefore compare the M07-B and AM04 potentials with results from the M07 potential at both the same PKA energy (10 keV), and the TDE-corrected equivalent energy of 16.6 keV (which produces the same surviving FP count as a 10 keV cascade in M07-B). For 10 keV cascades, the peak damage, relaxation time, and final FP counts are clearly lowest in the original M07 potential. For the 16.6 keV cascades, even though the final defect count is identical to the 10 keV cascades in M07-B, the peak damage is higher and the relaxation time longer, similar to the AM04 potential. Hence, despite the observed direct correlation between TDEs and surviving FP counts for the M07 and M07-B potentials, the early stages of cascades at equivalent TDE-normalised PKA energies are different. Clearly, this is to be expected when modifying the shape of the repulsive part of the potential. In terms of the stiffness parameters in Table 2, the M07 potential is softest and therefore expected to predict the strongest heat spike. However, even at the TDE-corrected 16.6 keV energy, the peak damage is at the same level as for 10 keV cascades in the AM04 potential, as seen in Fig. 7. This can be explained by the difference in melting temperatures, the AM04 potential predicts a lower melting point, resulting in a larger melted cascade region and consequently higher numbers of detected FPs at peak time. Our observations can therefore be summarised by concluding that the expected nature of the cascade can be predicted based on the threshold displacement energies and the stiffness of the repulsive potential, combined with the predicted melting point in the potential.

Fig. 8 shows the interstitial and vacancy cluster distributions after single 100 keV cascades in the different potentials. The surviving clusters from all simulations are grouped into bins and normalised by the number of simulations (50) to show the average number of clusters of a given size after a single cascade. For interstitials, the AM04 potential clearly produces more larger clusters, which in some cases form dislocation loops with Burgers vectors 1/2⟨111⟩. No ⟨100⟩ loops were observed for any PKA energy or potential. The interstitial cluster distribution of the M07-B and

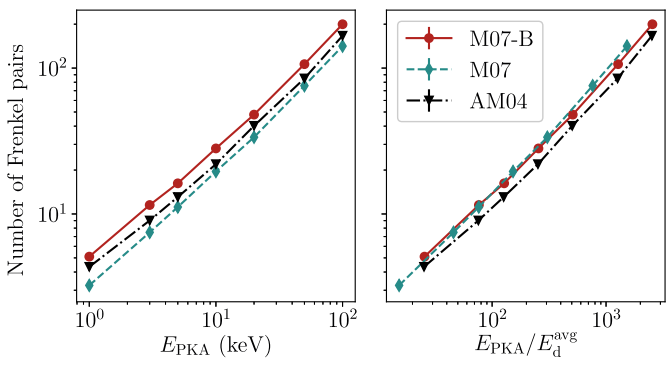

Fig. 6. Surviving numbers of Frenkel pairs as a function of PKA energy (left) and PKA energy divided by the average threshold displacement energy in the different potentials (right), for collision cascades at 0 K.

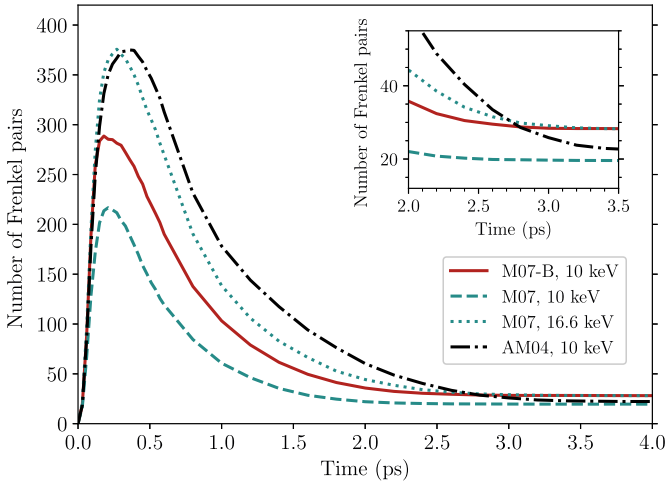

Fig. 7. Average number of Frenkel pairs as a function of time in 10 keV single cascade simulations in the different potentials. The 16.6 keV cascades in the M07 potential correspond to the energy equivalent to 10 keV cascades in the M07-B and AM04 potentials when normalised by the threshold displacement energy.

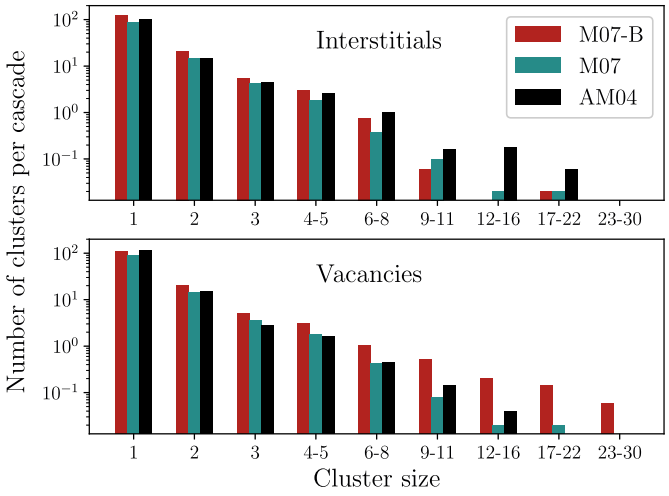

Fig. 8. Interstitial and vacancy cluster distributions for 100 keV single cascades.

M07 potentials are similar, with very few larger clusters. Interestingly, the vacancy clustering is on the other hand noticeably different between the potentials. Here, the AM04 potential only produces small clusters, while the M07-B potential predicts formation of larger vacancy clusters, sometimes in the shape of nano-sized voids or dislocation loop-like clusters. Unlike the interstitial cluster distribution, for vacancies there is also a clear difference between the M07-B and the M07 potential. The M07 potential does not produce large vacancy clusters to the same extent as the M07-B potential. Vacancy clustering has previously been suggested to correlate with the melting point, where a lower melting point was seen to lead to more clustering of vacancies [6,39]. However, the melting points are identical for the M07 and the M07-B potential, and cannot explain the difference in vacancy clustering. Furthermore, all migration, formation, and binding energies of vacancies and vacancy clusters are precisely the same in both potentials. The difference in vacancy clustering must therefore be due to differences in the dynamics of the early stages of the cascade, controlled by the repulsive parts of the potentials.

3.4. Overlapping cascade simulations

Fig. 9 shows the Frenkel pair evolution in the three different potentials as a function of number of cascades as well as a function of dose. If only the number of cascades are accounted for, we clearly observe different behaviour in all the potentials. In the very beginning, up to a few tens of cascades, the amount of Frenkel pairs is increasing almost linearly and according to the amount of defects produced in a single cascade. This is the region where no or very little cascade overlap has occurred. After about 50 cascades, we can see a deviation from this, when overlap effects become significant, and all potentials show a different behaviour. The AM04 potential starts first to deviate from the linear increase and the M07 potentials later. The M07 potentials start to deviate after the same number of cascades, but at different Frenkel pair levels. This difference between the M07 potentials can be explained by the different TDEs, which is clear when the number of Frenkel pairs is plotted against the dose. In the dose graph, the defect evolution is exactly the same in both M07 potentials, but they differ from the AM04 potential. This means that the damage produced in single isolated cascades does not define the evolution during continuous irradiation after a certain dose is reached, and consequently the effects of an improved short-range potential are less pronounced. After the critical dose is reached (about 0.02 dpa), the damage evolution is primarily controlled by the mobility and stability of dislocation loops and other defect clusters, which are identical in the M07 potentials and explain the similar trend. The small difference between the M07 potentials are mainly due to stochastic differences between the different simulation runs.

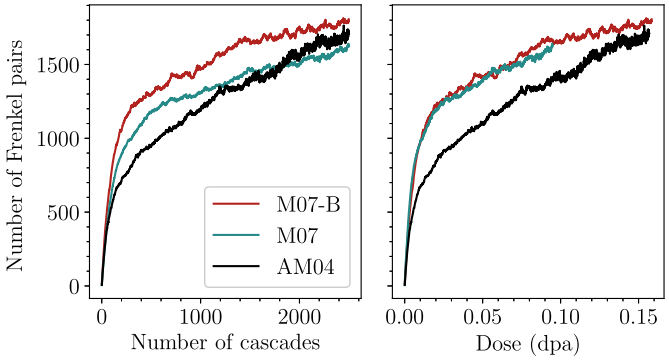

Fig. 9. Number of Frenkel pairs as a function of number of cascades (left) and dose (right) for cumulative 5 keV cascades at 300 K.

The differences in the total damage evolution between the potentials were studied in more detail by looking at the defect cluster evolution. The number of interstitials and vacancies in different-sized clusters can be seen in Fig. 10 and Fig. 11. For interstitials, large clusters are forming in the AM04 potential already at very low doses, similar to the results of the single cascades. This evolution is seen throughout the simulations, where large dislocation loops are forming and rapidly growing. There are some differences between the M07 potentials, but they seem to be more stochastic, as the formation of large loops from a combination of two smaller loops is case-dependent. A movie of the complete cascade series in all potentials can be found in the supplementary material, where every frame up to 2500 overlapping cascades are depicted to visualise the differences between the potentials. From this movie, it is clear that dislocation loops are easier formed and are more mobile in the AM04 potential. This leads to formation of large dislocation loops, that then govern the whole evolution of the system by absorbing any nearby smaller clusters. In the M07 potentials, we see more smaller, less mobile defect clusters. Many of these smaller clusters are identified as three-dimensional C15-like structures, which the M07 potentials correctly predict to be very stable. C15 clusters were

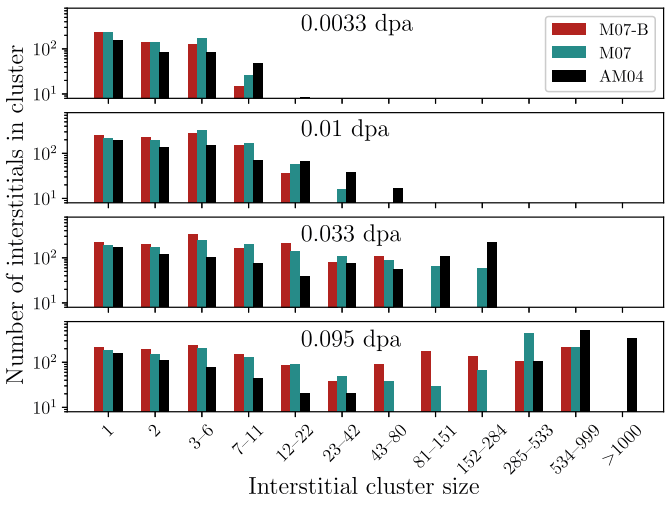

Fig. 10. Average number of interstitials in clusters of given sizes at different doses.

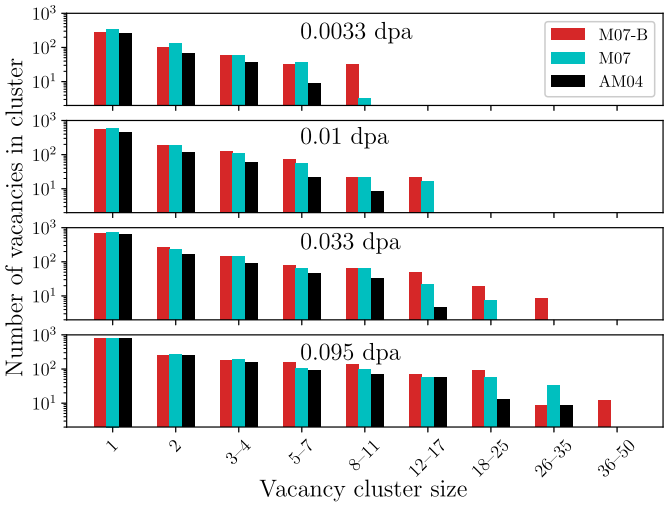

Fig. 11. Average number of vacancies in clusters of given sizes at different doses.

automatically identified as clusters made up of ⟨110⟩ dumbbells connected as hexagonal rings and triangles lying in ⟨111⟩ planes, as seen in Fig. 12(c). The automatically identified clusters were confirmed to be C15-like by visual inspection.

The frequent formation and growth of C15-like clusters in the M07 potentials has two important consequences on the total damage evolution. Firstly, the formation of C15-like clusters competes with the formation of dislocation loops, both of which are low in energy compared to other defect configurations, leading to significant populations of both types of clusters. Secondly, the C15 clusters are immobile and can trap nearby dislocation loops and therefore limit the growth rate of individual dislocation loops.

For vacancies, we also see a similar trend as in the single cascades. At low doses, there are more vacancy clusters in the M07-B potential than in the original M07 potential, which both show larger vacancy clusters than the AM04 potential. At higher doses, we see larger vacancy clusters in both the M07 potentials compared to the AM04, however, the difference between the M07 potentials is not as evident. This again suggests that after a certain dose, the defect cluster energetics are more important than the accuracy of the repulsive short-range potential.

The dislocation loops produced by the continuous irradiation are mainly of interstitial $1/2\langle 111\rangle$ type, but we also observed formation of $\langle 100\rangle$ loops according to the mechanisms described in Ref. [11]. Occasionally, vacancy loops of both types are also observed. Vacancy loops are more frequent in the M07 potentials, but can also be seen in the AM04 potential. Fig. 12 summarises the results from the overlapping cascades, where the defect structures in the M07-B and AM04 potential are shown at a dose of 0.095 dpa. Here, the large dislocation loops formed in the AM04 potential are visible, with otherwise only small clusters. On the other hand, the M07-B potential shows a larger amount of medium-sized clusters, with more and smaller dislocation loops than in the AM04 potential. The clusters identified as C15-like clusters are coloured orange.

3.5. Comparison between the M07-B and the AM04 potentials for cascade simulations

Here, we briefly summarise the differences between the new M07-B potential and the AM04 potential for properties relevant in cascade simulations. The formation and migration energies of single interstitials and vacancies are similar in both potentials, and in good agreement with *ab initio* data [14]. Some differences, however, appear in the properties of defect clusters. Most noteworthy is the more accurate description of the C15 Laves phase clusters in the M07-B potential [15]. The differences in stability of small three-dimensional defect clusters will, as our results have shown, have a strong effect on the surviving cascade damage. For dislocation loops, on the other hand, the M07-B potential predicts a crossover in stability between the two types ($1/2\langle 111\rangle$ and $\langle 100\rangle$ loops) at a size of around 100 interstitials [14], above which $\langle 100\rangle$ loops have a lower formation energy than $1/2\langle 111\rangle$ loops. In the AM04 potential, $1/2\langle 111\rangle$ loops are lower in energy for all sizes, in agreement with predictions based on *ab initio* data [40]. Another noteworthy difference between the potentials is the predicted melting temperatures. The AM04 potential reproduces the experimental melting point with good accuracy (1750 K vs. 1811 K [14]), while the M07-B potential overestimates the melting temperature by 25%. A more thorough comparison of the near-equilibrium properties is done in Ref. [14].

For properties dependent on the repulsive parts of the potentials, the M07-B potential is in overall better agreement with experimental and *ab initio* data. The threshold displacement energies are similar in both potentials, but the short-range many-body interactions are more accurately described in the M07-B potential (Fig. 5). Furthermore, the atomistic dynamics at short

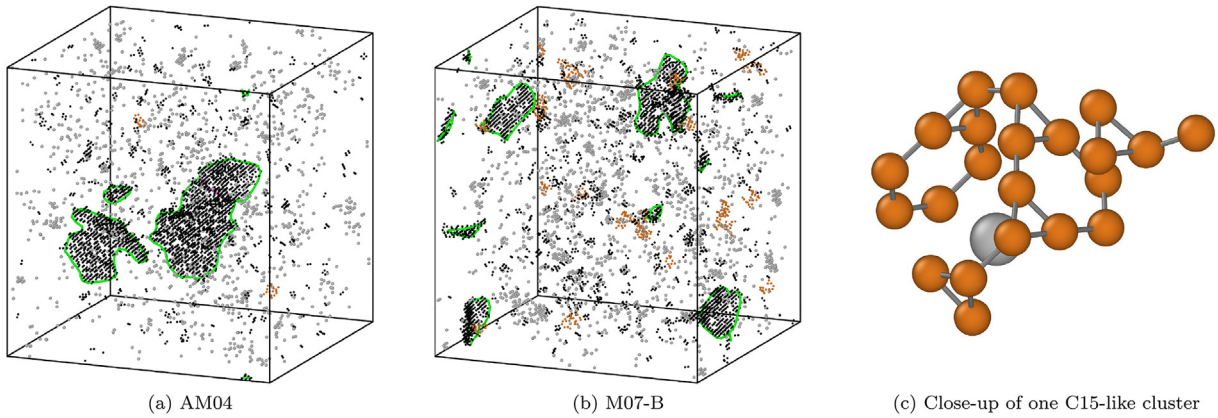

Fig. 12. Snapshots showing the interstitials and vacancies at 0.095 dpa. (a) AM04 potential, (b) M07-B potential, and (c) close-up of one of the C15-like clusters in the M07-B potential. Interstitials are coloured black and vacancies light grey. Green lines are dislocation lines for loops with Burgers vectors $1/2\langle 111\rangle$ and pink lines are for the Burgers vectors $\langle 100\rangle$. Interstitial atoms in C15-like clusters are coloured orange. (For interpretation of the references to colour in this figure legend, the reader is referred to the Web version of this article.)

interatomic distances are entirely controlled by the universal ZBL potential in the M07-B potential. In contrast, the AM04 potential utilises a different screening length for the ZBL potential, as discussed previously. Additionally, the short-range interactions are affected by the embedding energy function in the AM04 potential. However, it remains unclear how much this affects the evolution of a collision cascade.

Although both potentials are of overall good accuracy and well-suited for radiation damage studies, the above differences should be considered when choosing potential for cascade simulations. In short, the M07-B potential provides an overall better description of short-range many-body interactions and the relative stability of small defect clusters (such as the C15 cluster), while the AM04 potential more accurately reproduces the melting point and relative stability of larger dislocation loops.

4. Conclusions

We have modified an existing embedded atom method potential that accurately reproduces the equilibrium and self-interstitial properties in bcc iron, to also reproduce the threshold displacement energies and many-body repulsive energy curves sensitive to short-range interactions. The modified potential is more suitable for radiation damage simulations than the original parametrisation. We used the modified potential in both single and overlapping collision cascade simulations, and discussed the effects of an improved repulsive potential on the cascade damage in both cases. The results were compared with another well-established potential for radiation damage in iron. We found that the number of Frenkel pairs produced in single cascades is directly correlated with the average threshold displacement energy, in agreement with standard models for radiation damage. The clustering of vacancies after a single cascade was observed to be affected by the stiffness of the repulsive part of the potential. In overlapping cascades, after a certain dose is reached, the effects of the short-range potential are less significant and the evolution of the cascade damage after subsequent cascades is controlled by the stability and mobility of defect clusters defined by the near-equilibrium part of the potential. The different stabilities predicted by the potentials for parallel and non-parallel defect clusters, such as dislocation loops and the C15-type clusters, have a strong effect on the evolution of the cascade damage at higher doses.

Data availability

The raw data required to reproduce these findings cannot be shared at this time as the data also forms part of an ongoing study. The processed data required to reproduce these findings cannot be shared at this time as the data also forms part of an ongoing study.

Acknowledgements

This work has been carried out within the framework of the EUROfusion Consortium and has received funding from the Euratom research and training programme 2014–2018 under grant agreemegsnt No 633053. The views and opinions expressed herein do not necessarily reflect those of the European Commission. Grants of computer capacity from CSC - IT Center for Science, Finland are gratefully acknowledged. J.B. acknowledges financial support from Svenska kulturfonden (Arvid och Greta Olins fond).

Appendix A. Potential parameters

The fitted parameters of the polynomial transition function in the modified pair potential in Eq. (1) are given in Tab. A.3. The parameters of the density function polynomial in Eq. (3) are given in Tab. A.4.

Table A.3
Parameters of the polynomial function in Eq. (1), joining the original equilibrium part with the ZBL potential in the M07-B potential.

Parameter	Value
r_1 (Å)	1.0
r_2 (Å)	2.05
a_0	257.76705778
a_1	− 3011.57634735
a_2	14837.35638428
a_3	− 39778.63201904
a_4	62189.06228638
a_5	− 55882.6711731
a_6	25923.75131226
a_7	− 4417.9932785

Table A.4
Parameters of the modified electron density function (Eq. (3)) of the M07-B potential.

Parameter	Value
$\psi_{\max}$	40.0
R_1 (Å)	1.15
R_2 (Å)	1.35
A_0	512.81075267
A_1	− 2116.31367297
A_2	2832.24850222
A_3	− 1198.18199852

Appendix B. Supplementary data

Supplementary data related to this article can be found at https://doi.org/10.1016/j.jnucmat.2018.06.005.

References

[1] M.S. Daw, M.I. Baskes, Phys. Rev. B 29 (1984) 6443–6453, https://doi.org/10.1103/PhysRevB.29.6443.
[2] S.M. Foiles, M.I. Baskes, M.S. Daw, Phys. Rev. B 33 (1986) 7983–7991, https://doi.org/10.1103/PhysRevB.33.7983.
[3] M.S. Daw, S.M. Foiles, M.I. Baskes, Mater. Sci. Rep. 9 (1993) 251–310, https://doi.org/10.1016/0920-2307(93)90001-U.
[4] J.F. Ziegler, J.P. Biersack, U. Littmarck, In: Treatise on Heavy-ion Science, 1985, pp. 93–129. Pergamon.
[5] K. Nordlund, M. Ghaly, R.S. Averback, M. Caturla, T. Diaz de la Rubia, J. Tarus, Phys. Rev. B **57** (1998) 7556–7570, https://doi.org/10.1103/PhysRevB.57.7556.
[6] C. Björkas, K. Nordlund, Nucl. Instrum. Meth. Phys. Res. B 259 (2007) 853–860, https://doi.org/10.1016/j.nimb.2007.03.076.
[7] R.E. Stoller, A. Tamm, L.K. Béland, G.D. Samolyuk, G.M. Stocks, A. Caro, L.V. Slipchenko, Y.N. Osetsky, A. Aabloo, M. Klintenberg, Y. Wang, J. Chem. Theor. Comput. 12 (2016) 2871–2879, https://doi.org/10.1021/acs.jctc.5b01194.
[8] J. Tersoff, Phys. Rev. B 37 (1988) 6991–7000, https://doi.org/10.1103/PhysRevB.37.6991.
[9] A.E. Sand, J. Dequeker, C.S. Becquart, C. Domain, K. Nordlund, J. Nucl. Mater. 470 (2016) 119–127, https://doi.org/10.1016/j.jnucmat.2015.12.012.
[10] K. Vörtler, N. Juslin, G. Bonny, L. Malerba, K. Nordlund, J. Phys. Condens. Matter 23 (2011) 355007, https://doi.org/10.1088/0953-8984/23/35/355007.
[11] F. Granberg, J. Byggmästar, A.E. Sand, K. Nordlund, Europhys. Lett. 119 (2017) 56003, https://doi.org/10.1209/0295-5075/119/56003.
[12] F. Granberg, K. Nordlund, M.W. Ullah, K. Jin, C. Lu, H. Bei, L.M. Wang, F. Djurabekova, W.J. Weber, Y. Zhang, Phys. Rev. Lett. 116 (2016) 135504, https://doi.org/10.1103/PhysRevLett.116.135504.
[13] E. Levo, F. Granberg, C. Fridlund, K. Nordlund, F. Djurabekova, J. Nucl. Mater. 490 (2017) 323–332, https://doi.org/10.1016/j.jnucmat.2017.04.023.
[14] L. Malerba, M.C. Marinica, N. Anento, C. Björkas, H. Nguyen, C. Domain, F. Djurabekova, P. Olsson, K. Nordlund, A. Serra, D. Terentyev, F. Willaime, C.S. Becquart, J. Nucl. Mater. 406 (2010) 19–38, https://doi.org/10.1016/j.jnucmat.2010.05.017.

[15] M.-C. Marinica, F. Willaime, J.-P. Crocombette, Phys. Rev. Lett. 108 (2012) 025501, https://doi.org/10.1103/PhysRevLett.108.025501.
[16] G.J. Ackland, M.I. Mendelev, D.J. Srolovitz, S. Han, A.V. Barashev, J. Phys. Condens. Matter 16 (2004) S2629–S2642, https://doi.org/10.1088/0953-8984/16/27/003.
[17] M.I. Mendelev, S. Han, D.J. Srolovitz, G.J. Ackland, D.Y. Sun, M. Asta, Philos. Mag. A 83 (2003) 3977–3994, https://doi.org/10.1080/14786430310001613264.
[18] G.J. Ackland, D.J. Bacon, A.F. Calder, T. Harry, Philos. Mag. A 75 (1997) 713–732, https://doi.org/10.1080/01418619708207198.
[19] J. Lindhard, V. Nielsen, M. Scharff, Kgl Dan Vidensk Selsk Mat-Fys Medd 36 (1968), 31p.1968.
[20] G. Lucas, L. Pizzagalli, Nucl. Instrum. Meth. Phys. Res. B 229 (2005) 359–366, https://doi.org/10.1016/j.nimb.2004.12.119.
[21] P. Olsson, C.S. Becquart, C. Domain, Mater. Res. Lett. 4 (2016) 219–225, https://doi.org/10.1080/21663831.2016.1181680.
[22] M. Ghaly, K. Nordlund, R.S. Averback, Philos. Mag. A 79 (1999) 795–820, https://doi.org/10.1080/01418619908210332.
[23] A.H. Larsen, J.J. Mortensen, J. Blomqvist, I.E. Castelli, R. Christensen, Marcin Dułak, J. Friis, M.N. Groves, B. Hammer, C. Hargus, E.D. Hermes, P.C. Jennings, P.B. Jensen, J. Kermode, J.R. Kitchin, E.L. Kolsbjerg, J. Kubal, Kristen Kaasbjerg, S. Lysgaard, J.B. Maronsson, T. Maxson, T. Olsen, L. Pastewka, Andrew Peterson, C. Rostgaard, J. Schiøtz, O. Schütt, M. Strange, K.S. Thygesen, Tejs Vegge, L. Vilhelmsen, M. Walter, Z. Zeng, K.W. Jacobsen, J. Phys. Condens. Matter 29 (2017) 273002, https://doi.org/10.1088/1361-648X/aa680e.
[24] S. Plimpton, J. Comput. Phys. 117 (1995) 1–19, https://doi.org/10.1006/jcph.1995.1039. http://lammps.sandia.gov.
[25] K. Nordlund, J. Wallenius, L. Malerba, Nucl. Instrum. Meth. Phys. Res. B 246 (2006) 322–332, https://doi.org/10.1016/j.nimb.2006.01.003.
[26] F. Maury, M. Biget, P. Vajda, A. Lucasson, P. Lucasson, Phys. Rev. B 14 (1976) 5303–5313, https://doi.org/10.1103/PhysRevB.14.5303.
[27] H.J.C. Berendsen, J.P.M. Postma, W.F. van Gunsteren, A. DiNola, J.R. Haak, J. Chem. Phys. 81 (1984) 3684–3690, https://doi.org/10.1063/1.448118.
[28] K. Nordlund, Comput. Mater. Sci. 3 (1995) 448–456, https://doi.org/10.1016/0927-0256(94)00085-Q.
[29] M.J. Norgett, M.T. Robinson, I.M. Torrens, Nucl. Eng. Des. 33 (1975) 50–54, https://doi.org/10.1016/0029-5493(75)90035-7.
[30] S. Zhang, K. Nordlund, F. Djurabekova, F. Granberg, Y. Zhang, T.S. Wang, Mater. Res. Lett. 5 (2017) 433–439, https://doi.org/10.1080/21663831.2017.1311284.
[31] A. Stukowski, V.V. Bulatov, A. Arsenlis, Model. Simulat. Mater. Sci. Eng. 20 (2012) 085007, https://doi.org/10.1088/0965-0393/20/8/085007.
[32] A. Stukowski, Model. Simulat. Mater. Sci. Eng. 18 (2010) 015012, https://doi.org/10.1088/0965-0393/18/1/015012. http://ovito.org/.
[33] W.M. Haynes, CRC Handbook of Chemistry and Physics, 96th ed., CRC Press, Boca Raton, FL, 2015.
[34] F. Ercolessi, O. Tomagnini, S. Iarlori, E. Tosatti, in: Nanosources and Manipulation of Atoms under High Fields and Temperatures: Applications, NATO ASI Series, Springer, Dordrecht, 1993, pp. 185–205, https://doi.org/10.1007/978-94-011-1729-6_16.
[35] J.N. Lomer, M. Pepper, Philos. Mag. J. Theor. Exp. Appl. Phys. 16 (1967) 1119–1128, https://doi.org/10.1080/14786436708229961.
[36] C.S. Becquart, A. Souidi, M. Hou, Phys. Rev. B 66 (2002), https://doi.org/10.1103/PhysRevB.66.134104.
[37] D. Terentyev, C. Lagerstedt, P. Olsson, K. Nordlund, J. Wallenius, C.S. Becquart, L. Malerba, J. Nucl. Mater. 351 (2006) 65–77, https://doi.org/10.1016/j.jnucmat.2006.02.020.
[38] K. Nordlund, S.J. Zinkle, A.E. Sand, F. Granberg, R.S. Averback, R. Stoller, T. Suzudo, L. Malerba, F. Banhart, W.J. Weber, F. Willaime, S.L. Dudarev, D. Simeone, Nat. Commun. 9 (2018) 1084, https://doi.org/10.1038/s41467-018-03415-5.
[39] K. Nordlund, R.S. Averback, Phys. Rev. B 59 (1999) 20–23, https://doi.org/10.1103/PhysRevB.59.20.
[40] R. Alexander, M.-C. Marinica, L. Proville, F. Willaime, K. Arakawa, M.R. Gilbert, S.L. Dudarev, Phys. Rev. B 94 (2016) 024103, https://doi.org/10.1103/PhysRevB.94.024103.